F-actin organization and target constriction during primary macrophage phagocytosis is balanced by competing activity of myosin-I and myosin-II

Sarah R. Barger[a,†,‡], Daan Vorselen[b,c,‡,*], Nils C. Gauthier[d], Julie A. Theriot[b], and Mira Krendel[a,*]
[a]Department of Cell and Developmental Biology, State University of New York Upstate Medical University, Syracuse, NY 13210; [b]Department of Biology and Howard Hughes Medical Institute, University of Washington, Seattle, WA 98195; [c]Cell Biology and Immunology, Wageningen University and Research, Wageningen, the Netherlands; [d]IFOM, FIRC Institute of Molecular Oncology, Milan, Italy

ABSTRACT **Phagocytosis requires rapid remodeling of the actin cytoskeleton for extension of membrane protrusions and force generation to ultimately drive the engulfment of targets. The detailed mechanisms of phagocytosis have almost exclusively been studied in immortalized cell lines. Here, we make use of high-resolution imaging and novel biophysical approaches to determine the structural and mechanical features of phagocytosis by primary bone marrow–derived macrophages. We find that the signature behavior of these primary cells is distinct from macrophage-like cell lines; specifically, it is gentle, with only weak target constriction and modest polarization of the F-actin distribution inside the phagocytic cup. We show that long-tailed myosins 1e/f are critical for this organization. Deficiency of myo1e/f causes dramatic shifts in F-actin localization, reducing F-actin at the phagocytic cup base and enhancing F-actin–mediated constriction at the cup rim. Surprisingly, these changes can be almost fully reverted upon inhibition of another myosin motor protein, myosin-II. Hence, we show that the biomechanics and large-scale organization of phagocytic cups is tightly regulated through competing contributions from myosin-Ie/f and myosin-II.**

Monitoring Editor
Peter Van Haastert
University of Groningen

Received: Jun 13, 2022
Revised: Sep 9, 2022
Accepted: Sep 14, 2022

INTRODUCTION

Phagocytosis is a central process in cell biology, critical for tissue development and homeostasis (Boada-Romero *et al.*, 2020). Phagocytic targets are marked by ligands on their surface that bind and activate a variety of receptors on a phagocyte, which leads to complete engulfment and subsequent degradation of the target (Flannagan *et al.*, 2012). Macrophages are highly efficient phagocytes and as such are now being leveraged in immunotherapeutic strategies to fight cancer. Using antibodies to induce anti-cancer antibody-dependent cellular phagocytosis, as well as engineering chimeric phagocytic receptors to specifically target cancer cells, are both promising strategies for adapting macrophage phagocytosis for cancer treatment (Feng *et al.*, 2019; Chen *et al.*, 2021). These recent translational advances underscore the importance of understanding the underlying mechanisms of phagocytosis in a physiological setting.

Examining phagocytosis in vivo is challenging, yet multiple groups have made recent advances. Imaging of *Drosophila*, zebrafish, and mouse embryos has revealed a conserved role for phagocytosis in clearance of apoptotic cells, which is critical for proper development (Davidson and Wood, 2020; Hoijman *et al.*, 2021). In vitro, the use of immortalized macrophage-like cell lines enables easy manipulation and live-cell imaging, making primary macrophage phagocytosis far less studied. Some groups have utilized

This article was published online ahead of print in MBoC in Press (http://www.molbiolcell.org/cgi/doi/10.1091/mbc.E22-06-0210) on September 21, 2022.

‡These authors contributed equally to this work.

†Present address: Molecular, Cellular and Developmental Biology, Yale University, New Haven, CT 06511.

*Address correspondence to: Mira Krendel (krendelm@upstate.edu); Daan Vorselen (daan.vorselen@wur.nl).

Abbreviations used: BMDM, bone marrow–derived macrophages; DAAMPs, deformable acrylamide–coacrylic acid microparticles; FcR, Fc receptor; LLSM, lattice light-sheet microscopy.

primary macrophages to test the necessity of specific proteins and cell surface receptors for phagocytosis (Rotty *et al.*, 2017; Walbaum *et al.*, 2021), but the detailed structural organization of phagocytic cups and mechanical progression of primary macrophage phagocytosis remains unknown.

Mechanically, phagocytosis begins with active protrusive forces from the phagocyte in the form of membrane extensions, such as dorsal ruffles or pseudopodia, that make contact with the target. The target is then pulled closer to the phagocyte via these extensions, which continue to grow around the target surface to form a phagocytic cup (Vorselen *et al.*, 2020a; Mylvaganam *et al.*, 2021). The extending pseudopodia of the phagocytic cup are powered by polymerizing branched actin that pushes against the plasma membrane and accumulates in distinct foci ("teeth"; Barger *et al.*, 2019; Ostrowski *et al.*, 2019; Vorselen *et al.*, 2021). During pseudopod extension, significant cytoskeletal forces are also transmitted to the target, leading to constriction of the target (Vorselen *et al.*, 2021). Together, this makes the phagocytic cup a large and highly dynamic cytoskeletal structure, which is regulated by a multitude of actin-binding proteins, including Arp2/3 and multiple myosin motor proteins (May *et al.*, 2000; Barger *et al.*, 2020; Mylvaganam *et al.*, 2021). Recently, we established a clear role of myosin-II in mediating target constriction at the cup rim in RAW macrophages, and showed that long-tailed class I myosins, myosin 1e and myosin 1f, localize to protrusive F-actin spots (Vorselen *et al.*, 2021). Yet how these myosins coordinate the overall F-actin dynamics, and, therefore, the required forces for successful phagocytosis, remains largely unknown, especially for primary macrophages.

Here, we utilize microparticle traction force microscopy (MP-TFM) and lattice light-sheet microscopy (LLSM) to examine the mechanical forces underlying primary macrophage phagocytosis by Fc receptors (FcRs). The combination of these techniques has previously revealed complex spatiotemporal force exertions in the form of Arp2/3-nucleated protrusive actin teeth and myosin-II–mediated constriction in RAW macrophages (Vorselen *et al.*, 2021). We find that primary macrophages derived from murine bone marrow significantly differ from macrophage-like cell lines in their phagocytic force signature. Phagocytic uptake by primary cells is gentler and linked to a more even distribution of F-actin between the rim and base of the phagocytic cup. Surprisingly, this cytoskeletal organization and force distribution of the phagocytic cup is balanced by competing contributions of nonmuscle myosin-II and myosins 1e/f.

RESULTS AND DISCUSSION

Target constriction is decoupled from phagocytic cup progression during phagocytosis in primary macrophages

To study the mechanical process of phagocytosis by primary macrophages, we generated murine bone marrow–derived macrophages (BMDMs) and challenged them to engulf deformable acrylamide–coacrylic acid microparticles (DAAMPs) with a Young's modulus of 0.3 kPa, functionalized with bovine serum albumin (BSA) and anti–BSA antibody, to monitor phagocytic forces during FcR–mediated phagocytosis (Vorselen *et al.*, 2020b). The use of deformable hydrogel microparticles enabled us to challenge primary cells with targets of similar stiffness to those quantified for apoptotic or cancerous cells (Van der Meeren *et al.*, 2020). Furthermore, mapping deformations on the DAAMP target allowed us to analyze forces applied by the macrophage to characterize the mechanical signature of primary cell phagocytic uptake. Imaging by LLSM enabled excellent 3D resolution of phagocytosis with low phototoxicity. Primary phagocytes were transfected with Halo-Lifeact and dyed with JF646 (Janelia Fluor 646 HaloTag Ligand) to visualize the actin cytoskeleton. Similar to our previous studies using RAW macrophages (Vorselen *et al.*, 2021), the primary macrophages readily internalized the soft targets, but with some notable differences in internalization behavior. The primary macrophages exhibited significantly more actin-rich plasma-membrane ruffles preceding internalization and surrounding the formation of the phagocytic cup (Figure 1A). During phagocytosis, this included F-actin structures that do not necessarily follow the particle surface (Figure 1A, green arrowheads), sometimes containing branches that grow perpendicular to the main pseudopod (Figure 1A, cyan arrowheads), and are sometimes sharply bent (Figure 1A, pink arrowheads). While recent studies utilizing volumetric imaging by LLSM have highlighted the presence and complexity of such surface ruffles (Condon *et al.*, 2018; Quinn *et al.*, 2021), they appear to be a consistent feature of phagocytosis in primary cells as compared with RAW macrophages, whose protrusions seem to almost exclusively closely follow the particle surface in antibody-mediated phagocytosis. The ruffling activity observed in primary macrophages may have been stimulated by the continuous presence of M-CSF in the medium (Racoosin and Swanson, 1989). However, the concentration of M-CSF used in our imaging experiments is lower than that typically utilized for inducing ruffling, and it appears likely that the ruffling activity stimulated by M-CSF would have been subdued due to the continuous exposure to the growth factor rather than acute stimulation.

We then examined deformations on the DAAMP target due to forces applied by the primary macrophages to investigate the pattern and timing of target constriction. Similarly to the RAW macrophages, the primary macrophages constricted the DAAMP targets during uptake, as indicated by a narrow band of inward deformation (~200 nm on average) that moved along the target over time (Figure 1, B and C). Constriction occurred specifically at regions of elevated actin intensity within the phagocytic cup (Figure 1B). In RAW cells, these normal forces applied to the target coincided with the Arp2/3 complex–nucleated actin teeth (Vorselen *et al.*, 2021). Similarly, distinct protrusive spots mediated target deformation in BMDMs. However, in contrast to RAW cells, where target constriction and teeth activity took place primarily at the rim of the phagocytic cup, in primary cells, target constriction (~200 nm) often did not coincide with the location of the phagocytic cup rim (Figure 1, D and E). By examining the progression of the phagocytic cup and time of maximum target constriction, we identified an average delay of ~40 s between cup rim progression and constriction in primary cells using LLSM (Figure 1E). This altered distribution of force generation over the course of internalization suggests a unique mechanical signature of phagocytosis in primary macrophages.

Phagocytic uptake by primary macrophages involves low overall force exertion but high activity at the base of the phagocytic cup

To better understand this mechanical difference in phagocytic uptake by primary cells, we investigated the actin cytoskeleton organization in fixed BMDMs engulfing DAAMPs and stained with fluorescently labeled phalloidin. 3D reconstructions of the DAAMP target enabled us to localize cell-induced deformations at high spatial resolution, while immunostaining of the exposed target allowed for precise staging of internalization (Figure 2, A and B; Vorselen *et al.*, 2020b). First, we challenged BMDMs to ingest DAAMPs of 1.4 kPa, which surprisingly resulted in negligible deformations, suggesting the targets were too stiff for the cells to deform. To note, we had previously been able to easily identify deformations of 1.4 kPa targets produced by RAW macrophages, which exerted total forces of 1–20 nN (Vorselen *et al.*, 2021). In an attempt to still characterize the

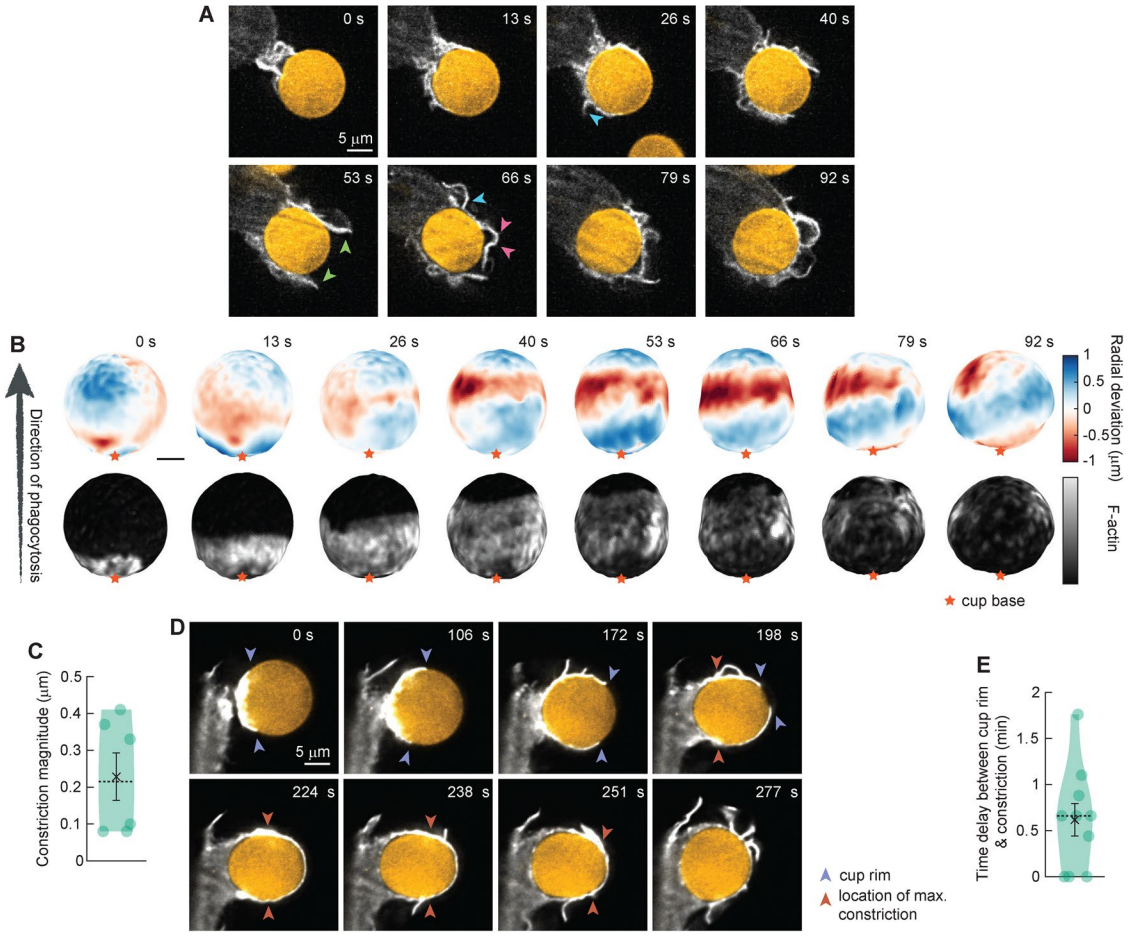

FIGURE 1: Lattice light-sheet microscopy (LLSM) imaging reveals decoupling of pseudopod progression and target constriction in FcR–mediated phagocytosis by BMDMs. Bone marrow–derived macrophages (BMDMs) transfected with Halo-Lifeact and dyed with JF646 were fed soft deformable acrylamide–coacrylic acid micro (DAAM) particles (~13 µm, 0.3 kPa) functionalized with IgG and Alexa Fluor 488 cadaverine and imaged using LLSM. (A) Time-lapse montage (min:s) of optical slices in *x*/*y*. Arrowheads indicate F-actin branches (cyan), pseudopods detached from the particle surface (green), and sharply bent pseudopods (pink). (B) Side view of the DAAM-particle internalized in A and reconstructed with superresolution accuracy, showing target deformations and F-actin localization on particle surface. Colorscale represents the deviation of each vertex from a perfect sphere with radius equal to the median radial distance of edge coordinates to the particle centroid. (C) Maximum constriction during phagocytosis. For each event, the frame with maximal target constriction was used. (D) Time-lapse montage (min:s) of optical slices in *x*/*z* showing large lag (~100 s) between progression of the cup rim and constriction. (E) Time lag between cup rim and constriction passing 50% engulfment for 10 events. Violin plots show individual phagocytic events (circles), mean (black cross), standard error of the mean (error bars), and median (dashed line).

biophysical behavior of primary macrophages, we exposed BMDMs to softer DAAMPs, with a Young's modulus of 0.3 kPa. Using these softer targets, we observed clear global target deformations, evaluated by target sphericity (Figure 2C and Supplemental Figure 1). To readily compare individual phagocytic cups, they were aligned along the phagocytic axis, defined as the axis from the centroid of the cell-target contact area through the target centroid to the opposing target surface (Figure 2D). Interestingly, this revealed another difference between RAW cell and BMDM phagocytosis regarding the typical orientation of cups. Whereas RAW cell cups form parallel to the coverslip as well as vertically from the coverslip (~46° angle with the coverslip on average), BMDM cups were almost exclusively formed growing up (~69° on average for 1.4 kPa particles; Figure 2E). This observation could simply reflect shape differences between BMDMs, which are often fairly spread out, and RAW cells, which generally retain a more rounded shape. Alternatively, this could also indicate a greater reliance on dorsal ruffles for target capture in the primary macrophages.

By averaging the F-actin distribution of all the phagocytic cups along the phagocytic axis, we detected a slight accumulation of F-actin toward the front of the phagocytic cup (Figure 2F). However, the location of the F-actin intensity peak did not correlate with the site of generation of inward normal forces, as illustrated by quantifying the radial deviation of the DAAMP. Instead, this analysis revealed that primary macrophages are pushing on the target at the base of the phagocytic cup as visible in individual particle reconstructions (Figure 2B, top and middle rows) and shown by the change in the radial deviation of the target (Figure 2F, right panel). This pushing results in an overall compression along the phagocytic axis, which is even noticeable for 1.4 kPa DAAMPS, and is clearly distinct from the elongation along this axis observed for RAW macrophages (Figure 2G). During phagocytosis, it is believed that F-actin is cleared from

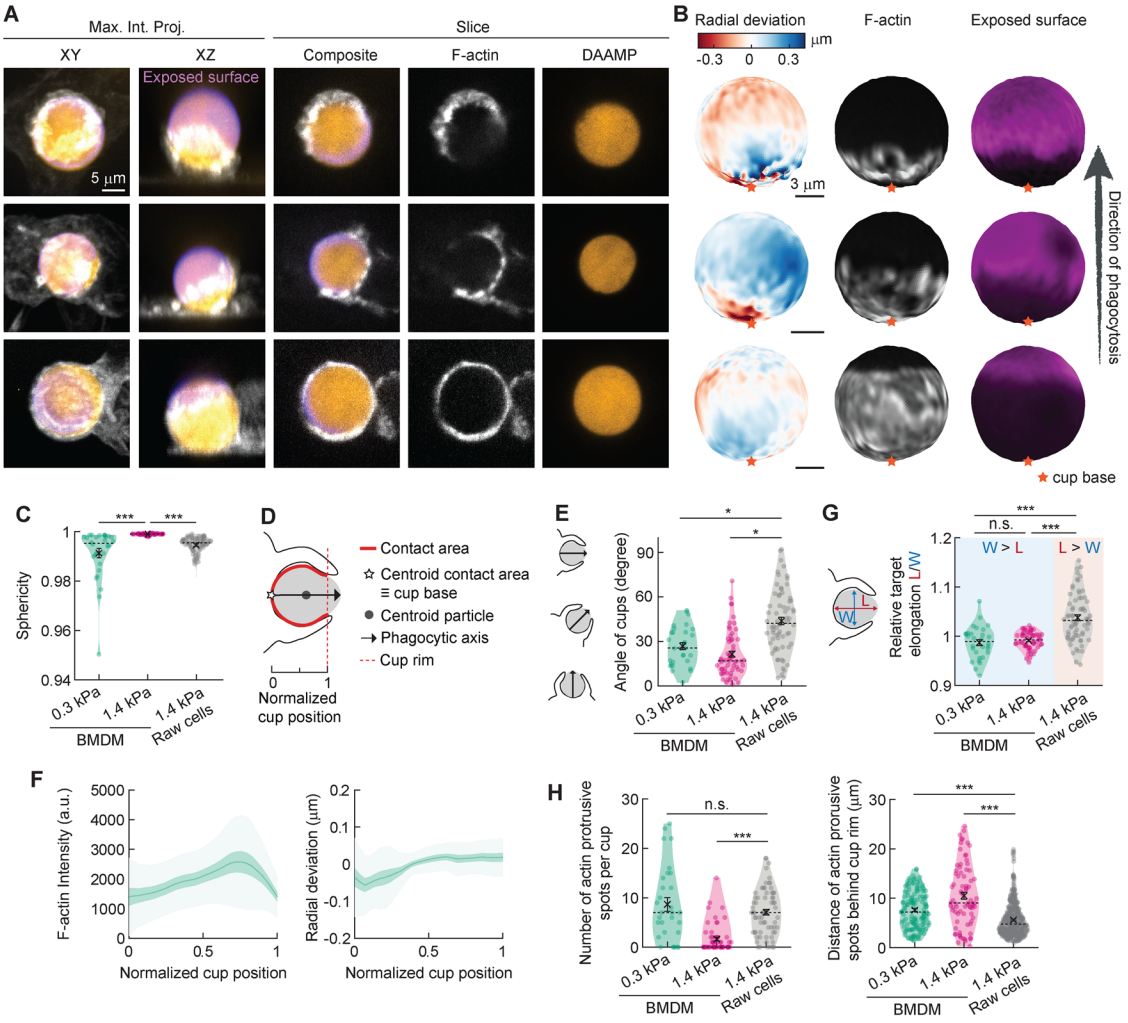

FIGURE 2: Phagocytosis by BMDMs is gentle and involves local pushing at the cup base. (A) Confocal images of fixed BMDMs phagocytosing soft (~13 µm, 0.3 kPa) deformable acrylamide–coacrylic acid microparticles (DAAMPs) functionalized with IgG, and AF488-cadaverine for visualization. Cells were stained for F-actin and labeled with a fluorescent secondary antibody to reveal the exposed surface of the target. Left two columns: composite maximum intensity projections (MIPs) of confocal stacks; third to fifth column: single confocal slices (*xy*). (B) 3D shape reconstructions of DAAMPs in A revealing detailed target deformations induced during phagocytosis and localization of F-actin over the particle surface. (C) Target sphericity indicating total target deviation from a spherical shape, where 1 would be an undeformed perfect sphere. (D) Schematic representation of phagocytic parameterization. Normalized cup position indicates the relative position along the phagocytic axis between the cup base (0) and 1. (E) Direction of the phagocytic axis, where 0° indicates straight up from and 90° parallel to the coverslip. (F) Average profiles of target deformation and F-actin intensity along the phagocytic axis, where 0 and 1 are the cup base and rim, respectively. Signals were first averaged in rings over the surface along the phagocytic axis on a per-particle basis. Only targets beyond 40% engulfment were included (19 out of 30 events). (G) Relative elongation of particles undergoing phagocytosis. Wilcoxon signed rank test for differences with 1 (no compression or elongation) were performed for each sample, showing target compression for 0.3 ($p = 0.047$) and 1.4 kPa particles ($p = 0.002$) for BMDMs, and target elongation ($p = 2 \times 10^{-7}$) for RAW macrophages. (H) Number and localization of actin-containing protrusive spots per cup. All violin plots show individual phagocytic events (colored circles), mean (black cross), and median (dashed line), and all error bars indicate standard error of the mean. Unless otherwise indicated, statistical tests were two-sided Wilcoxon rank sum test with *, $p < 0.05$ and ***, $p < 0.001$. Data on RAW macrophages was taken from previously published work (Vorselen *et al.*, 2021).

the base of the phagocytic cup to recycle F-actin–regulating factors or to make room for vesicle docking by focal exocytosis, effectively increasing the surface area of the phagocyte (Scott *et al.*, 2005; Schlam *et al.*, 2015). Yet, our high-resolution imaging of F-actin distribution throughout the phagocytic cup in BMDMs shows little evidence for significant F-actin clearance with little change in F-actin intensity over normalized position along the cup (Figure 2, B and F).

Our observations of no clear target constriction and only subtle F-actin accumulation at the rim of the phagocytic cup support our initial observations by live-cell LLSM imaging. These data together suggest that local pushing on the target at the base of the phagocytic cup in primary cells is actin based, which seems counterintuitive for successful uptake. This behavior is markedly different from RAW macrophages ingesting 1.4 kPa DAAMPs analyzed in a similar

manner (Vorselen *et al.*, 2021), where F-actin accumulation was five-fold greater at the rim of the phagocytic cup than at the base, and accounted for significant local target deformation.

Despite this more even distribution of F-actin within the phagocytic cup of primary cells, the previously reported F-actin foci, or teeth, were evident by confocal imaging (Figure 2A; Vorselen *et al.*, 2021). We identified and quantified actin teeth within the phagocytic cup based on their protrusive nature and high F-actin intensity. As expected, BMDMs formed significantly fewer teeth per phagocytic cup when exposed to the stiffer 1.4 kPa DAAMPs (Figure 2H). However, when challenged to engulf the softer targets (0.3 kPa), BMDMs formed roughly the same number of actin teeth per phagocytic cup as RAW macrophages for 1.4 kPa targets. Interestingly, the location of BMDM teeth was much more variable throughout the phagocytic cup, whereas RAW macrophages mainly assembled actin teeth close to the cup rim (Vorselen *et al.*, 2021). This variability in localization of protrusive teeth is in line with the lack of distinct constriction at the rim of the phagocytic cup. Overall, our direct mechanical comparison between RAW macrophages and BMDMs reveals clear differences in internalization behavior between macrophage-like cell lines and primary macrophages.

Myosins 1e/f regulate F-actin coupling to the membrane and target constriction

We had previously reported that myosin-Is, specifically myosin 1e (myo1e) and myosin 1f (myo1f), uniquely localize to the tips of force-producing actin teeth within the phagocytic cup (Barger *et al.*, 2019; Vorselen *et al.*, 2021). When myo1e/f are knocked out simultaneously, BMDMs exhibit excessive actin polymerization and deficient phagocytic internalization of stiff polystyrene beads (Barger *et al.*, 2019). To test how these myosins regulate the mechanical forces underlying phagocytic internalization, we utilized BMDMs lacking both myosin-Is, given their previously reported functional redundancy in phagocytosis (Barger *et al.*, 2019). We challenged wild-type (WT) and myo1e/f double-knockout (dKO) BMDMs to ingest 0.3 kPa DAAMPs and fixed phagocytic cups for target deformation analysis (Figure 3, A and B, and Supplemental Figure 1). Interestingly, we found that dKO macrophages produced a force signature similar to that of nontransfected RAW macrophages, which express myo1f at comparable levels to WT BMDMs, and myo1e at slightly lower levels (Barger *et al.*, 2019). In particular, in the phagocytic cups of dKO BMDMs, F-actin accumulated in a narrow band near the front of the cup, which colocalized with the maximal inward deformation of the DAAMPs (Figure 3, A–C). While peak F-actin intensity within the phagocytic cups of WT and dKO cells did not differ, the lack of myosin-Is led to diminished F-actin inside the phagocytic cup, suggesting a role for myo1e/f in maintaining F-actin at the base of phagocytic cups (Figure 3, D and E). These differences in F-actin accumulation also reflected changes in phagocytic forces. Notably, while overall magnitude of target deformation did not differ from the WT macrophages (Figure 3F), dKO macrophages exhibited altered force exertion patterns with significantly greater constriction at the rim of the phagocytic cup (Figure 3H). Past efforts to quantify phagocytic forces using planar traction force microscopy (TFM) on an IgG-coated surface revealed no change in exerted shear forces upon myosin-I loss (Barger *et al.*, 2019). However, our current utilization of DAAMPs, which allows quantification of normal forces in addition to shear forces, reveals that myo1e/f negatively regulate target constriction within the phagocytic cup.

We had previously shown that loss of these myosin-Is results in excessive accumulation of branched actin networks when macrophages are stimulated for FcR–mediated internalization (Barger *et al.*, 2019). Likewise, we find here that phagocytic actin teeth in dKO macrophages were significantly larger in diameter and their position shifted to the rim of the phagocytic cup (Figure 3, I and J). This data suggests that myo1e/f regulates target constriction through regulating the size and positioning of protrusive teeth, either at the cup rim or more broadly throughout the phagocytic cup.

In light of this interesting role for myosin-Is in negatively regulating force generation during phagocytosis, we wanted to test whether this behavior was maintained on stiffer targets, especially because the effects of myo1e/f on F-actin distribution inside the phagocytic cup and on phagocytic force exertion have not been previously described. Although phagocytosis has been well characterized as a mechanosensitive process (Beningo and Wang, 2002; Sosale *et al.*, 2015; Vorselen *et al.*, 2020b), the specific molecular players involved in mechanosensing remain largely unknown (Jaumouillé and Waterman, 2020; Vorselen *et al.*, 2020a), especially in the antibody-mediated uptake in which integrins do not play a dominant role at high opsonin concentrations (Lim *et al.*, 2007; Freeman *et al.*, 2016). Surprisingly, comparing phagocytic cups formed on the stiffer 1.4 kPa targets revealed little difference in F-actin distribution between WT and dKO macrophages, with no clear shift of F-actin from inside the cup to the cup rim (Figure 3, K–M). Although deficiency of myo1e/f resulted in a qualitatively similar shift of F-actin teeth to the rim of the phagocytic cup as observed on softer targets (Figure 3N), this also did not result in changed target deformation for the 1.4 kPa targets. This finding suggests that myo1e/f perform a mechanosensitive function, adjusting F-actin organization and target constriction specifically when phagocytes are presented with soft targets.

Myosins 1e/f and myosin-II have opposing effects on F-actin organization within the phagocytic cup of primary macrophages

Multiple aspects of the phagocytic behavior of the myosin 1e/f dKO BMDMs seem to be the opposite of the phenotype previously reported for myosin-II inhibition in RAW macrophages, including the shift in F-actin distribution and the effect on target constriction (Vorselen *et al.*, 2021). This made us eager to examine the effect of myosin-II inhibition in BMDMs. Using RAW macrophages, we have previously found that when myosin-II was inhibited, F-actin at the phagocytic cup rim was diminished, with F-actin instead more spread out to the base of the cup, which ultimately reduced target constriction (Vorselen *et al.*, 2021). To test whether myosin-II performs a similar role during phagocytosis of soft targets in primary macrophages, we treated BMDMs with blebbistatin to inhibit myosin-II activity and challenged them to ingest 0.3 kPa DAAMPs. We observed modest changes in F-actin distribution within the phagocytic cup that were consistent with our previous observations in RAW macrophages (Figure 4A). Specifically, while peak F-actin intensity within the cup did not differ, there was a distinct broadening of the F-actin signal (Figure 4, B and C). This small change in the organization of the actin cytoskeleton was also accompanied by a reduction in the total target deformation, but no clear effect on target constriction could be detected (Figure 4D). Thus, although myosin-II may still regulate force generation through the regulation of F-actin distribution or disassembly within the phagocytic cup, it appears to play a less significant role than in RAW macrophages.

Because myosin-Is negatively regulate target constriction by altering the location of F-actin teeth within the phagocytic cup, we speculated that myosin-II perturbation could reverse this effect. We thus treated dKO macrophages with dimethyl sulfoxide (DMSO) or blebbistatin and exposed them to 0.3 kPa DAAMPs. Intriguingly,

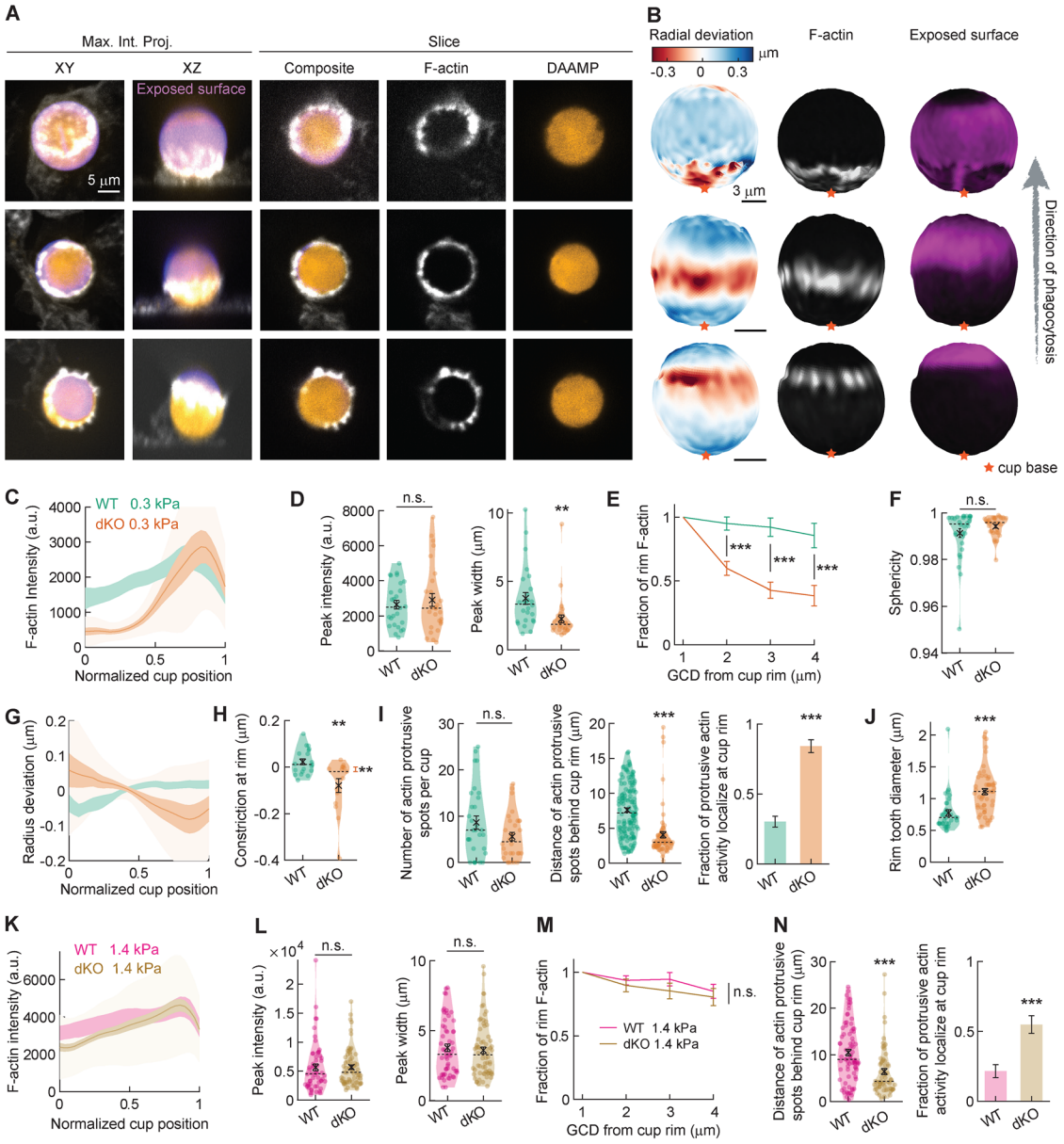

FIGURE 3: Myosin-Ie/f inhibits target constriction and regulates F-actin coupling in a mechanosensitive manner. (A) Confocal images of fixed myo1e$^{-/-}$, myo1f$^{-/-}$ dKO macrophages phagocytosing soft (~13 μm, 0.3 kPa) deformable acrylamide–coacrylic acid microparticles (DAAMPs) functionalized with IgG, and AF488-cadaverine for visualization. Cells were stained for F-actin and labeled with a fluorescent secondary antibody to reveal the exposed surface of the target. Left two columns: composite maximum intensity projections (MIPs) of confocal stacks; third to fifth column: single confocal slices (*xy*). (B) 3D shape reconstructions of DAAMPs in A revealing detailed target deformations induced during phagocytosis and localization of F-actin over the particle surface. (C) Average profile of F-actin intensity along the phagocytic axis, where 0 and 1 are the cup base and rim, respectively. Intensity was first averaged in rings over the surface along the phagocytic axis on a per-particle basis. Only targets beyond 40% engulfment were included (19 out of 30 WT events and 15 out of 30 dKO events). (D) Maximum F-actin intensity and full-width at half maximum (FWHM) of the F-actin peak. (E) F-actin intensity deeper inside the cup as a function of great circle distance to the cup rim (GCD: distance measured along the surface of the sphere) to the cup rim. (F) Target sphericity indicating total target deviation from a spherical shape, where 1 would be an undeformed perfect sphere. (G) Average profiles of target deformation along the phagocytic axis (as in C for F-actin intensity). (H) Constriction at cup rim. Only significant constriction was observed for dKO cells (one-sided one-sample Wilcoxon signed rank test: $p = 0.92$ and $p = 0.005$ for WT and dKO cells, respectively). (I) Left, number and localization of actin-containing protrusive spots per cup. Right, fraction of protrusive F-actin activity localized at the front of the cup. Fisher's exact test was used for comparing absolute numbers ($p = 5 \times 10^{-12}$). (J) Size of protrusive F-actin spots localized at the cup rim. (K–N) Similar to C, D, E, and I, but for 11.3 μm, 1.4 kPa targets. (J) 46 out of 58 WT events and 46 out of 52 dKO events beyond 40% engulfment events were used. (N) Fisher's exact test was used for comparing absolute numbers underlying the bar graph ($p = 4 \times 10^{-4}$). All violin plots show individual phagocytic events (colored circles), mean (black cross), and median (dashed line), and all error bars indicate standard error of the mean. All statistical tests were two-sided Wilcoxon rank sum test with *, $p < 0.05$; **, $p < 0.01$; and ***, $p < 0.001$ unless indicated otherwise.

blebbistatin treatment reversed the F-actin profile of phagocytic cups in the dKO macrophages, making them appear similar to WT macrophages. F-actin no longer accumulated at the rim of the phagocytic cup and became significantly broader throughout the cup (Figure 4, F–H). This redistribution of F-actin at the rim of the cup led to lower overall target deformation and less constriction at the rim specifically (Figure 4, I and J). While blebbistatin treatment did not alter the number or the larger diameter of the actin teeth observed in dKO macrophages, it did rescue their altered positioning (Figure 4, K–M). When myosin-II was inhibited, protrusive actin teeth in the dKO macrophages were more broadly distributed throughout the phagocytic cup, similar to the WT macrophages. Together, these data reveal that myosin-I and myosin-II have opposing effects on key morphological and biophysical aspects of phagocytic cup formation, including F-actin organization, actin teeth positioning, and target constriction (Figure 4N). In previous work (Vorselen *et al.*, 2021), we have shown that in RAW cells, myosin-I and myosin-II exhibit distinct localization patterns, with myosin-II localizing to circumferential actin belts slightly behind the rim of the phagocytic cups, whereas myosins-Ie/f localize at actin teeth at the edge of the cup. These localization differences may reflect differing roles for the two types of myosin motors.

CONCLUSIONS

Overall, we report that primary macrophages exhibit a gentle form of phagocytic uptake, characterized by only a slight constriction of the target, which is decoupled from the extension of the phagocytic cup. This behavior contrasts remarkably with that of the often-utilized macrophage-like cell lines and is explained by a broader distribution of F-actin inside the phagocytic cup. F-actin teeth in primary cells are also more evenly positioned throughout the phagocytic cup, thereby generating less localized constricting forces at the cup rim. Using primary knockout macrophages and chemical inhibition, we elucidate the role of the two myosin classes that are highly expressed in primary phagocytes. We demonstrate that inhibition of myosin-II mildly broadens F-actin organization in the phagocytic cup and slightly reduces the cell's ability to deform its target. This modest effect of the myosin-II inhibition may support previous work in which myosin-II inhibition did not significantly affect the internalization efficiency of stiff targets by BMDMs (Rotty *et al.*, 2017). In contrast, we discover that deletion of myosin-Is, myo1e/f, dramatically shifts the F-actin network in primary cells, diminishing F-actin at the base of the phagocytic cup and enhancing F-actin–mediated constriction at the cup rim. This disrupted patterning also includes the occurrence of larger F-actin teeth, specifically situated at the rim of the cup. Interestingly, this effect is mechanosensitive, and is most clearly observed when BMDMs are fed softer targets.

Intriguingly, the effect of myosin 1e/f deficiency can be reversed upon myosin-II inhibition, revealing that F-actin organization and target constriction in the phagocytic cup is balanced by competing contributions of myosin-I and myosin-II activity (Figure 4N). How might myosin-I and myosin-II be organizing the F-actin network and force generation antagonistically? It's possible that myosin-Is, as membrane-cytoskeletal linkers, are coupling the F-actin network to the plasma membrane throughout the phagocytic cup. Loss of these myosins has been shown to lower membrane tension by reducing membrane-cytoskeleton adhesion (Barger *et al.*, 2019), which may enhance F-actin polymerization once stimulated (Houk *et al.*, 2012; Diz-Muñoz *et al.*, 2016). Inhibiting myosin-II has been shown to decrease cortical tension and therefore elevate membrane tension (Gauthier *et al.*, 2011; Houk *et al.*, 2012). Thus, blebbistatin treatment in the dKO macrophages may result in increased membrane tension, thereby reducing—and rescuing—the effects of concentrated F-actin polymerization and constriction at the phagocytic cup rim. Alternatively, myosin-I and myosin-II typically occupy different actin networks (i.e., branched actin for myosin-I and anti-parallel bundles for myosin-II) within the cell (Reymann *et al.*, 2012; McIntosh and Ostap, 2016; Shutova and Svitkina, 2018). It is possible that the balance of these actin networks (branched vs. anti-parallel bundles) within the phagocytic cup is maintained by myosin-I and myosin-II and that altering this balance results in a shift in their relative contribution to force exertion in phagocytosis. Furthermore, if these motors apply specific forces on these networks that regulate other actin effector proteins, then the identity and dynamics of these networks may be altered. Further work is necessary to determine which of these explanations underlie the apparent competition in F-actin network architecture and force exertion between myosin 1e/f and myosin-II, and whether this competition extends to other dynamic cellular shape changes.

MATERIALS AND METHODS

Request a protocol through *Bio-protocol*.

Animals

A description of the myo1e$^{-/-}$; myo1f$^{-/-}$ dKO mice has been previously published (Barger *et al.*, 2019). All mice used in this study were maintained on a C57BL/6 background. All procedures utilizing mice were performed according to the animal protocols approved by the IACUC of SUNY Upstate Medical University under the IACUC protocol 364 and in compliance with all applicable ethical regulations. Both male and female mice were used; for each individual experiment utilizing BMDMs, bone marrow preparations from age- and sex-matched mice were used.

Bone marrow isolation and cell culture

Following euthanasia, femurs and tibias of mice were removed and flushed with DMEM containing 10% fetal bovine serum (FBS) and 1% antibiotic–antimycotic (Life Technologies; cDMEM). Red blood cells were lysed using ACK buffer (0.15 M NH_4Cl). Bone marrow progenitor cells were recovered by centrifugation (250 × *g*, 5 min, 4°C), washed once with sterile phosphate-buffered saline (PBS), and plated on tissue culture dishes in a 37°C incubator with 5% CO_2. The next day, nonadherent cells were moved to bacteriological (non-tissue-culture–treated) Petri dishes and differentiated over 1 wk in cDMEM containing 20 ng/ml recombinant murine M-CSF (Biolegend; 576404). All experiments were done within 5 days post-differentiation. RAW264.7 (ATCC; male murine cells) were cultured in DMEM, high glucose, containing 10% FBS and 1% antibiotic–antimycotic at 37°C with 5% CO_2.

Chemicals and drugs

Blebbistatin (original version) was purchased from EMD Millipore. Alexa Fluor 568–conjugated phalloidin was purchased from Life Technologies. Janelia Fluor 646 (JF646) HaloTag Ligand was a generous gift from Luke Lavis (Janelia Research Campus).

Phagocytosis assays

DAAMPs were added to a total volume of 400 µl of serum-free DMEM, briefly sonicated in a bath sonicator, and applied to phagocytes in a 12-well plate. To synchronize phagocytosis and initiate DAAMP–phagocyte contact, the plate was spun at 300 × *g* for 3 min at 4°C. Cells were incubated at 37°C to initiate phagocytosis for a period of 5 min. Media was then removed and cells were fixed with 4% paraformaldehyde/PBS for 15 min. Any unbound DAAMPs were

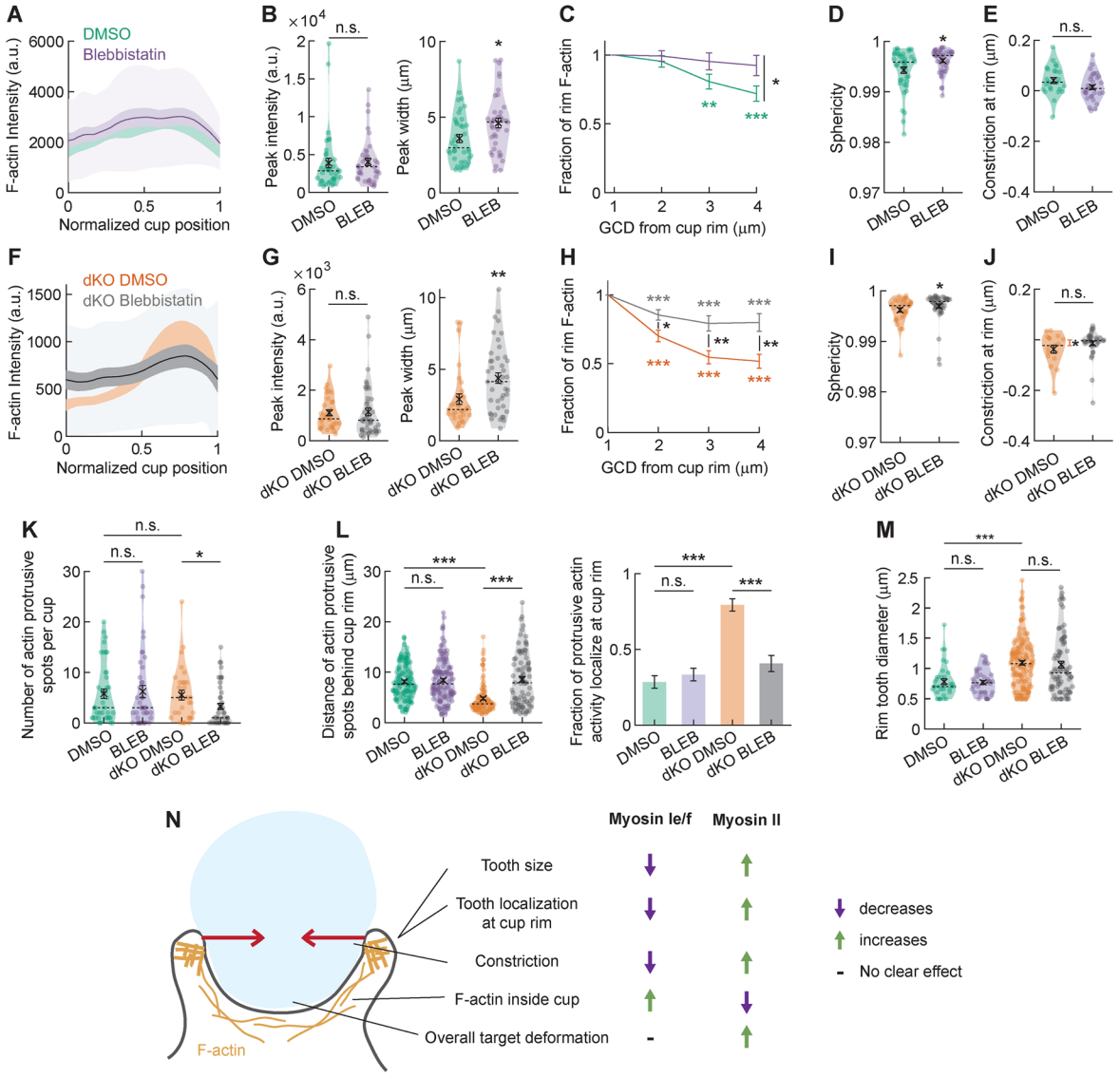

FIGURE 4: Myosins-1e/f and myosin-II inversely regulate F-actin distribution within the phagocytic cup during internalization. (A) Average profile of F-actin intensity along the phagocytic axis in phagocytic cups formed by DMSO and blebbistatin-treated BMDM phagocytosing soft (~13 μm, 0.3 kPa) deformable acrylamide–coacrylic acid microparticles (DAAMPs) functionalized with IgG. 0 and 1 indicate the cup base and rim, respectively. Intensity was first averaged in rings over the surface along the phagocytic axis on a per-particle basis. Only targets beyond 40% engulfment were included (24 out of 41 DMSO events and 31 out of 42 blebbistatin events). (B) Maximum F-actin intensity and full-width at half maximum (FWHM) of the F-actin peak. (C) F-actin intensity inside the cup as a function of GCD to the cup rim. (D) Target sphericity indicating total target deviation from a spherical shape, where 1 would be an undeformed perfect sphere. (E) Constriction at cup rim. No significant constriction was observed for either sample (one-sided one-sample Wilcoxon signed rank test: 1 and 0.89 for DMSO and blebbistatin-treated cells, respectively). (F–J) Similar to A–E, but for DMSO and blebbistatin-treated myo1e$^{-/-}$ myo1f$^{-/-}$ dKO BMDMs showing that blebbistatin treatment largely reverses the dKO phenotype. (F) 17 out of 31 DMSO events and 35 out of 44 dKO events beyond 40% engulfment events were used. (J) Only significant constriction was observed for untreated cells (one-sided one-sample Wilcoxon signed rank test: $p = 0.021$ and $p = 0.22$ for DMSO and blebbistatin-treated cells, respectively). (K) Number of actin-containing protrusive spots per cup. (L) Location of F-actin–containing protrusive spots and fraction of protrusive F-actin activity localized at cup rim. (M) Diameter of F-actin–containing protrusive spots localized at the cup rim. Fisher's exact test was used for comparing absolute numbers underlying the bar graph, with $p = 0.47$ (n.s.) and $p = 4 \times 10^{-14}$ for blebbistatin-treated cells and dKO DMSO-treated cells compared with DMSO-treated WT cells, respectively. $p = 4 \times 10^{-7}$ for DMSO against blebbistatin-treated dKO cells. (M) Size of protrusive F-actin spots localized at the cup rim. (N) Schematic summary figure indicating the effects of myosins-Ie/f and myosin-II on F-actin organization and target deformation during phagocytosis. Some of the indicated effects (e.g., myosin-II effect on tooth size) are based on the previous results in RAW 264.7 macrophage-like cells (Vorselen *et al.*, 2021). All violin plots show individual phagocytic events (colored circles), mean (black cross), and median (dashed line), and all error bars indicate standard error of the mean. All statistical tests were two-sided Wilcoxon rank sum test with *, $p < 0.05$; **$p < 0.01$; and ***, $p < 0.001$ unless indicated otherwise.

then washed away with three washes of PBS and samples were stained with goat anti-rabbit–Alexa Fluor 405 antibodies (Invitrogen; A31556; 1:400) for 30 min to visualize exposed DAAMP area. Cells were then washed with PBS (three times for 5 min each) and permeabilized with 0.1% Triton X-100/PBS for 3 min, then stained with Alexa Fluor 568–conjugated phalloidin (1:300). Coverslips were then mounted using VECTASHIELD Antifade Mounting Medium (Vector Laboratories; H-1000) and sealed with nail polish. For drug treatments, cells were exposed to the indicated drug concentration for 30 min before the assay and DAAM particles were resuspended and exposed to cells in the same drugged media. Experiments described in the current article and in our previously published work (Vorselen *et al.*, 2021) were performed using the same DAAMP preparation (1.4 kPa DAAMPs) within a span of 2 mo, which allowed us to perform comparisons between the primary cell phagocytosis described here and the RAW cell phagocytosis described in Vorselen *et al.* (2021). All experiments using 0.3 kPa DAAMPs were also performed using a single DAAMP preparation.

Microscopy

Confocal images were taken using a PerkinElmer UltraView VoX Spinning Disc Confocal system mounted on a Nikon Eclipse Ti-E microscope equipped with a Hamamatsu C9100-50 EMCCD camera, a 60× (1.49 NA) PlanApo objective, and controlled by Volocity software. Images for protein localization were taken using a Leica TCS SP8 laser scanning confocal microscope with an HC Pl APO 63×/1.4 NA oil CS2 objective at the Upstate Medical University Leica Center of Excellence.

The LLSM (Chen *et al.*, 2014) utilized was developed by E. Betzig and operated/maintained in the Advanced Imaging Center at the Howard Hughes Medical Institute Janelia Research Campus (Ashburn, VA); 488, 560, or 642 nm diode lasers (MPB Communications) were operated between 40 and 60 mW initial power, with 20–50% acousto-optic tunable filter transmittance. The microscope was equipped with a Special Optics 0.65 NA/3.75 mm water dipping lens, excitation objective, and a Nikon CFI Apo LWD 25× 1.1 NA water dipping collection objective, which used a 500-mm focal length tube lens. Macrophages were imaged in a 37°C-heated, water-coupled bath in FluoroBrite medium (Thermo Scientific) supplemented with Glutamax, 0–5% FBS, 1% Pen/Strep, and 10 ng/mL M-CSF. Opsonized DAAMPs were added directly to the media bath before acquisition. Images were acquired with a Hamamatsu Orca Flash 4.0 V2 sCMOS camera in custom-written LabView Software. Postimage deskewing and deconvolution was performed using Howard Hughes Medical Institute (HHMI) Janelia custom software and 10 iterations of the Richardson-Lucy algorithm.

Microparticle synthesis

DAAM particles were synthesized using an extrusion-based emulsification process as previously described (Vorselen *et al.*, 2020b). Gel premixtures containing 100 mg/ml acrylic components, 150 mM NaOH, 0.3% (vol/vol) tetramethylethylenediamine, and 150 mM MOPS (prepared from MOPS sodium salt, pH 7.4) were prepared. Mass fraction of acrylic acid was 10%, while cross-linker mass fraction was 0.3% and 0.65% for 0.3 kPa and 1.4 kPa particles, respectively. The gel mixture was degassed for 15 min and then kept under nitrogen atmosphere until and during extrusion. Tubular hydrophobic Shirasu porous glass (SPG) with 1.9-mm pore size were sonicated under vacuum in n-heptane, mounted on an internal pressure micro kit extruder (SPG Technology) and immersed into the oil phase (~125 ml) consisting of hexanes (99%) and 3% (vol/vol) Span 80 (Fluka; 85548). A gel mixture (10 ml) was extruded through SPG membranes under nitrogen pressure of ~7 kPa. The oil phase was kept under nitrogen atmosphere and stirred continuously at 300 rpm. After extrusion was completed, the emulsion temperature was increased to 60°C and subsequently polymerization was induced by the addition of ~225 mg 2,2′-azobisisobutyronitrile; 1.5 mg/ml final concentration). The polymerization reaction was continued for 3 h at 60°C and then at 40°C overnight. Polymerized particles were subsequently washed (five times in hexanes, one time in ethanol), dried under nitrogen flow for ~30 min, and resuspended in PBS (137 mM NaCl, 2.7 mM KCl, 8.0 mM Na_2HPO_4, 1.47 mM KH_2PO_4, pH 7.4). They were stored at 4°C until use. Typical particle preparations have low variability in particle diameter (coefficient of variation [CV] of ~0.1) and in polymer density (CV 0.03–0.05, as evaluated by refractive index measurements; Vorselen *et al.*, 2020b).

Microparticle functionalization

DAAM particles were functionalized as previously detailed (Vorselen *et al.*, 2020b). Briefly, DAAMPs were diluted to 5% (vol/vol) concentration and washed twice in activation buffer (100 mM MES, 200 mM NaCl, pH 6.0). They were then incubated for 15 min in activation buffer supplemented with 40 mg/ml 1-ethyl-3-(3-dimethylaminopropyl) carbodiimide, 20 mg/ml N-hydroxysuccinimide (NHS), and 0.1% (vol/vol) Tween 20. Immediately after the final wash, the particles were resuspended in PBS, pH 8 with 20 mg/ml BSA (Sigma; A3059) and incubated at room temperature, rocking for 1 h. Cadaverine conjugate Alexa Fluor 488 cadaverine (Thermo Fisher Scientific; A-30679) was then added to a final concentration of 0.2 mM. After 30 min, unreacted NHS groups were blocked with 100 mM TRIS and 100 mM ethanolamine (pH 9). DAAMPs were then spun down (16,000 × *g*, 2 min) and washed four times in PBS, pH 7.4 with 0.1% Tween 20. BSA-functionalized DAAMPs were resuspended in PBS, pH 7.4 without Tween. Finally, DAAMPs were washed three times in sterile PBS and opsonized with 3 mg/ml rabbit anti–BSA antibody (MP Biomedicals; 0865111) for 1 h at room temperature. DAAMPs were then washed three times (16,000 × *g*, 2 min) with PBS and resuspended in sterile PBS.

3D target shape analysis and mapping of fluorescent signals

Volumetric images were analyzed to obtain superresolved 3D target shapes using custom Matlab software (Vorselen *et al.*, 2020b, 2021). Images were thresholded for an initial estimate of the volume and centroid of individual microparticles. Intensity values along lines originating from the particle centroid and crossing the particle edge approximately equidistantly were obtained by cubic interpolation. These lines were then used for determining edge coordinates with superresolution accuracy by fitting a Gaussian to their discrete derivative. Because the determination of particle properties such as sphericity and constriction is sensitive to high-frequency noise, edge coordinates were smoothed akin to a 2D moving average filter. Specifically, great circle distances between each pair of edge coordinates were calculated, and the radial component of the edge coordinates within the given window size was averaged (1 μm^2). A triangulation between edge coordinates was then generated, and the particle surface area S and volume V calculated. Sphericity was calculated as $\Psi = (6\pi^{1/3}V^{2/3}S^{-1})$. Similarly to edge coordinate determination, mapping of F-actin intensity and immunostaining was done by determining the fluorescent signals along radial lines originating from the particle centroid and passing through each edge coordinate using linear interpolation. The maximum value within 1 µm of the edge coordinate was projected onto the DAAMP surface.

Determination of cell-target contact area, phagocytic axis, and cup rim

The calculation of the fraction engulfed, angle of the phagocytic axis, alignment of particles along this axis, and obtaining the boundary of the cup to determine local constriction and F-actin signal as a function of distance from the cup rim, was performed using both the F-actin stain and immunostaining of the free particle surface (Vorselen *et al.*, 2020b, 2021). Both signals were binarized, initially by using a dip in the distribution of the logarithm of pixel intensities as the threshold. The mask was then further optimized using the F-actin signal and a region-based active contour (or snake) algorithm (Lankton and Tannenbaum, 2008). For determination of F-actin concentration relative to the cup rim as well as constriction at the cup rim, the "rim" signal was taken at a greater circle distance (GCD) of 2.5 μm behind this contour. For LLSM data, where no staining of the free particle surface was present, alignment was done manually.

ACKNOWLEDGMENTS

This work was supported by the American Heart Association under Grant no.18PRE34070066 to S.R.B., the National Institute of General Medical Sciences of the National Institutes of Health under Award no. R01GM-138652 to M.K., the Italian Association for Cancer Research (AIRC), Investigator Grant no. 20716 to N.C.G., and the Howard Hughes Medical Institute (J.A.T.). D.V. further acknowledges the Cancer Research Institute for support through a CRI Irvington fellowship. LLSM imaging was performed at the Advanced Imaging Center (AIC), HHMI Janelia Research Campus. We thank John M. Heddleston and Jesse Aaron of the AIC for help with imaging. The AIC is jointly funded by the Gordon and Betty Moore Foundation and the HHMI. We thank Sharon Chase for help with animal experiments.

REFERENCES

Barger SR, Gauthier NC, Krendel M (2020). Squeezing in a meal: myosin functions in phagocytosis. Trends Cell Biol 30, 157–167.

Barger SR, Reilly NS, Shutova MS, Li Q, Maiuri P, Heddleston JM, Mooseker MS, Flavell RA, Svitkina T, Oakes PW, *et al.* (2019). Membrane-cytoskeletal crosstalk mediated by myosin-I regulates adhesion turnover during phagocytosis. Nat Commun 10, 1249.

Beningo KA, Wang Y-L (2002). Fc-receptor-mediated phagocytosis is regulated by mechanical properties of the target. J Cell Sci 115, 849–856.

Boada-Romero E, Martinez J, Heckmann BL, Green DR (2020). The clearance of dead cells by efferocytosis. Nat Rev Mol Cell Biol 21, 398–414.

Chen S, Lai SWT, Brown CE, Feng M (2021). Harnessing and enhancing macrophage phagocytosis for cancer therapy. Front Immunol 12, 635173.

Chen BC, Legant WR, Wang K, Shao L, Milkie DE, Davidson MW, Janetopoulos C, Wu XS, Hammer JA 3rd, Liu Z, *et al.* (2014). Lattice light-sheet microscopy: imaging molecules to embryos at high spatiotemporal resolution. Science 346, 1257998.

Condon ND, Heddleston JM, Chew T-L, Luo L, McPherson PS, Ioannou MS, Hodgson L, Stow JL, Wall AA (2018). Macropinosome formation by tent pole ruffling in macrophages. J Cell Biol 217, 3873–3885.

Davidson AJ, Wood W (2020). Macrophages use distinct actin regulators to switch engulfment strategies and ensure phagocytic plasticity in vivo. Cell Rep 31, 107692.

Diz-Muñoz A, Thurley K, Chintamen S, Altschuler SJ, Wu LF, Fletcher DA, Weiner OD (2016). Membrane tension acts through PLD2 and mTORC2 to limit actin network assembly during neutrophil migration. PLoS Biol 14, e1002474.

Feng M, Jiang W, Kim BYS, Zhang CC, Fu YX, Weissman IL (2019). Phagocytosis checkpoints as new targets for cancer immunotherapy. Nat Rev Cancer 19, 568–586.

Flannagan RS, Jaumouille V, Grinstein S (2012). The cell biology of phagocytosis. Annu Rev Pathol 7, 61–98.

Freeman SA, Goyette J, Furuya W, Woods EC, Bertozzi CR, Bergmeier W, Hinz B, van der Merwe PA, Das R, Grinstein S (2016). Integrins form an expanding diffusional barrier that coordinates phagocytosis. Cell 164, 128–140.

Gauthier NC, Fardin MA, Roca-Cusachs P, Sheetz MP (2011). Temporary increase in plasma membrane tension coordinates the activation of exocytosis and contraction during cell spreading. Proc Natl Acad Sci USA 108, 14467–14472.

Hoijman E, Häkkinen H-M, Tolosa-Ramon Q, Jiménez-Delgado S, Wyatt C, Miret-Cuesta M, Irimia M, Callan-Jones A, Wieser S, Ruprecht V (2021). Cooperative epithelial phagocytosis enables error correction in the early embryo. Nature 590, 618–623.

Houk AR, Jilkine A, Mejean CO, Boltyanskiy R, Dufresne ER, Angenent SB, Altschuler SJ, Wu LF, Weiner OD (2012). Membrane tension maintains cell polarity by confining signals to the leading edge during neutrophil migration. Cell 148, 175–188.

Jaumouillé V, Waterman CM (2020). Physical constraints and forces involved in phagocytosis. Front Immunol 11, 1097.

Lankton S, Tannenbaum A (2008). Localizing region-based active contours. IEEE Trans Image Process 17, 2029–2039.

Lim J, Wiedemann A, Tzircotis G, Monkley SJ, Critchley DR, Caron E. (2007). An essential role for talin during $\alpha_M\beta_2$-mediated phagocytosis. Mol Biol Cell 18, 976–985.

May RC, Caron E, Hall A, Machesky LM (2000). Involvement of the Arp2/3 complex in phagocytosis mediated by FcγR or CR3. Nat Cell Biol 2, 246–248.

McIntosh BB, Ostap EM (2016). Myosin-I molecular motors at a glance. J Cell Sci 129, 2689–2695.

Mylvaganam S, Freeman SA, Grinstein S (2021). The cytoskeleton in phagocytosis and macropinocytosis. Curr Biol 31, R619–R632.

Ostrowski PP, Freeman SA, Fairn G, Grinstein S (2019). Dynamic podosome-like structures in nascent phagosomes are coordinated by phosphoinositides. Dev Cell 50, 397–410.e393.

Quinn SE, Huang L, Kerkvliet JG, Swanson JA, Smith S, Hoppe AD, Anderson RB, Thiex NW, Scott BL (2021). The structural dynamics of macropinosome formation and PI3-kinase-mediated sealing revealed by lattice light sheet microscopy. Nat Commun 12, 4838.

Racoosin EL, Swanson JA (1989). Macrophage colony-stimulating factor (rM-CSF) stimulates pinocytosis in bone marrow-derived macrophages. J Exp Med 170, 1635–1648.

Reymann A-C, Boujemaa-Paterski R, Martiel J-L, Guérin C, Cao W, Chin HF, De La Cruz EM, Théry M, Blanchoin L (2012). Actin network architecture can determine myosin motor activity. Science 336, 1310–1314.

Rotty JD, Brighton HE, Craig SL, Asokan SB, Cheng N, Ting JP, Bear JE (2017). Arp2/3 complex is required for macrophage integrin functions but is dispensable for FcR phagocytosis and in vivo motility. Dev Cell 42, 498–513.e496.

Schlam D, Bagshaw RD, Freeman SA, Collins RF, Pawson T, Fairn GD, Grinstein S (2015). Phosphoinositide 3-kinase enables phagocytosis of large particles by terminating actin assembly through Rac/Cdc42 GTPase-activating proteins. Nat Commun 6, 8623.

Scott CC, Dobson W, Botelho RJ, Coady-Osberg N, Chavrier P, Knecht DA, Heath C, Stahl P, Grinstein S (2005). Phosphatidylinositol-4,5-bisphosphate hydrolysis directs actin remodeling during phagocytosis. J Cell Biol 169, 139–149.

Shutova MS, Svitkina TM (2018). Mammalian nonmuscle myosin II comes in three flavors. Biochem Biophys Res Commun 506, 394–402.

Sosale NG, Rouhiparkouhi T, Bradshaw AM, Dimova R, Lipowsky R, Discher DE (2015). Cell rigidity and shape override CD47's "self"-signaling in phagocytosis by hyperactivating myosin-II. Blood 125, 542–552.

Van der Meeren L, Verduijn J, Krysko DV, Skirtach AG (2020). AFM analysis enables differentiation between Apoptosis, Necroptosis, and Ferroptosis in Murine Cancer Cells. iScience 23, 101816.

Vorselen D, Barger SR, Wang Y, Cai W, Theriot JA, Gauthier NC, Krendel M (2021). Phagocytic 'teeth' and myosin-II 'jaw' power target constriction during phagocytosis. Elife 10, e68627.

Vorselen D, Labitigan RLD, Theriot JA (2020a). A mechanical perspective on phagocytic cup formation. Curr Opin Cell Biol 66, 112–122.

Vorselen D, Wang Y, de Jesus MM, Shah PK, Footer MJ, Huse M, Cai W, Theriot JA (2020b). Microparticle traction force microscopy reveals subcellular force exertion patterns in immune cell–target interactions. Nat Commun 11, 20.

Walbaum S, Ambrosy B, Schütz P, Bachg AC, Horsthemke M, Leusen JHW, Mócsai A, Hanley PJ (2021). Complement receptor 3 mediates both sinking phagocytosis and phagocytic cup formation via distinct mechanisms. J Biol Chem 296, 100256.